Discovery of a Bimodal Environmental Distribution of Compact Ellipticals in the Local Universe

Guangwen Chen[1,2], Hong-Xin Zhang[1,2,6], Xu Kong[1,2,3,6], Zesen Lin[1,2], Zhixiong Liang[1,2], Zuyi Chen[4], Yimeng Tang[1,2,5], and Xinkai Chen[1,2]

[1] CAS Key Laboratory for Research in Galaxies and Cosmology, Department of Astronomy, University of Science and Technology of China, Hefei 230026, People's Republic of China; guangwen@mail.ustc.edu.cn
[2] School of Astronomy and Space Sciences, University of Science and Technology of China, Hefei, 230026, People's Republic of China; hzhang18@ustc.edu.cn
[3] Frontiers Science Center for Planetary Exploration and Emerging Technologies, University of Science and Technology of China, Hefei, Anhui, 230026, People's Republic of China; xkong@ustc.edu.cn
[4] Steward Observatory, University of Arizona, 933 N Cherry Avenue, Tucson, AZ 85721, USA
[5] Department of Astronomy and Astrophysics, University of California, Santa Cruz, 1156 High Street, Santa Cruz, CA 95064, USA

Abstract

Low-mass compact stellar systems (CSSs; $M_\star < 10^{10} M_\odot$) are thought to be a mixed bag of objects with various formation mechanisms. Previous surveys of CSSs were biased to relatively high-density environments and cannot provide a complete view of the environmental dependence of the formation of CSSs. We conduct the first-ever unbiased flux-limited census of nearby quiescent CSSs over a total sky area of $\sim$200 deg^2 observed by the GAMA spectroscopic survey. The complete sample includes 82 quiescent CSSs, of which 85% fall within the stellar mass range of classical compact ellipticals (cEs). By quantifying the local environment with the normalized projected distance $D/R_{\rm vir}$ to the nearest luminous neighboring galaxy, we find that these CSSs have a bimodal $D/R_{\rm vir}$ distribution, with one group peaking near $\sim 0.1 \times R_{\rm vir}$ (satellite) and the other peaking near $\sim 10 \times R_{\rm vir}$ (field). In contrast to the CSSs, ordinary quiescent galaxies of similar masses have a unimodal $D/R_{\rm vir}$ distribution. Satellite CSSs are older and more metal-rich than field CSSs on average. The bimodal $D/R_{\rm vir}$ distribution of quiescent CSSs reinforces the existence of two distinct formation channels (tidal stripping and born-to-be) for cEs and may be understood in two mutually inclusive perspectives, i.e., substantial tidal stripping happens only when satellite galaxies travel sufficiently close to their massive hosts, and there exists an excess of high-density cE-bearing subhalos close to massive halos.

Unified Astronomy Thesaurus concepts: Compact dwarf galaxies (281); Compact galaxies (285); Galaxy formation (595); Stellar populations (1622); Tidal interaction (1699); Elliptical galaxies (456)

1. Introduction

There exist a variety of compact stellar systems (CSSs) that lie in between classical globular clusters and ordinary galaxies in the size–luminosity plane ($10^6 \lesssim M_\star/M_\odot \lesssim 10^{10}$; $10 \lesssim R_{\rm e} \lesssim 600$ pc). Well-known types of CSSs include supermassive star clusters, ultracompact dwarfs (UCDs; Hilker et al. 1999; Drinkwater et al. 2000; Brodie et al. 2011), and compact ellipticals (cEs; Chilingarian et al. 2009; Huxor et al. 2013; Norris et al. 2014; Chilingarian & Zolotukhin 2015; Kim et al. 2020).

One prevailing scenario for the origin of these intermediate-mass CSSs is that they are the central remnants of tidally stripped nucleated galaxies. This scenario is motivated by the fact that many CSSs are spatially associated with more massive neighbor galaxies or lie in galaxy clusters/groups (e.g., Chilingarian et al. 2009; Price et al. 2009). Discoveries of tidal streams and overmassive central black holes in several CSSs support the tidal stripping scenario (e.g., Seth et al. 2014; Pechetti et al. 2022). A series of circumstantial evidence for this scenario has been found for the UCD system in the Virgo cluster (Liu et al. 2015a; Zhang et al. 2015). UCDs follow mass–metallicity relations similar to

nuclear star clusters, instead of ordinary globular clusters (Zhang et al. 2018). Alternatively, CSSs, especially those at the low-mass end, may be simply supermassive star clusters or their merger products (e.g., Fellhauer & Kroupa 2002; Mieske et al. 2012). Ordinary galaxies may evolve into compact galaxies through environmental regulation of star formation (Du et al. 2019). The discovery of apparently isolated cEs implies that they may be born to be compact galaxies (e.g., Huxor et al. 2013; Paudel et al. 2014; Rey et al. 2021), and some of them may be merger remnants of smaller galaxies (e.g., Paudel et al. 2014). Some group/cluster cEs may be ejected via a three-body interaction and become isolated (Chilingarian & Zolotukhin 2015).

Given their intermediate nature, it is conceivable that CSSs constitute a mixed bag of various formation mechanisms that depend on properties such as mass and environment. A vast majority of previous studies focused on CSSs located in relatively high-density environments (e.g., galaxy groups, clusters). Chilingarian & Zolotukhin (2015) and Kim et al. (2020) are among the few studies that selected large samples of cEs (195 and 138, respectively) over a large sky area that covers different environments, thanks to the Sloan Digital Sky Survey (SDSS; York et al. 2000).

Previous studies lack a complete (either in a volume-limited or flux-limited sense) and large-sky-area (covering a variety of environments) census of CSSs that allows for an unbiased investigation of the formation of CSSs. This is because most large-scale spectroscopic surveys such as SDSS suffer from the

---

[6] Corresponding authors.

fiber-collision problem, which severely affects the census of CSSs on small scales. The Galaxy and Mass Assembly spectroscopic survey (GAMA; Driver et al. 2011) largely overcomes the fiber-collision problem by adopting a multipass observing strategy. Moreover, GAMA significantly improves the completeness level of compact galaxies (Baldry et al. 2010). In this work, we perform the first flux-limited census of nearby CSSs based on the GAMA survey and study the structural properties and stellar populations of CSSs over different local environments. Throughout this work, we assume a flat ΛCDM cosmology with $\Omega_m = 0.3$, $\Omega_\Lambda = 0.7$, and $h_0 = 0.7$.

2. Sample Selection

2.1. Compact Stellar Systems

The latest data release of GAMA (DR4; Driver et al. 2022) covers three equatorial regions (field IDs: G09, G12, and G15) and two southern regions (field IDs: G02 and G23). The equatorial regions are 95% complete down to $r \simeq 19.7$ mag. The G02 and G23 fields are complete down to $r \simeq 19.8$ and 19.4 mag, respectively. The GAMA collaboration did not observe galaxy candidates that meet their selection criteria but had already been observed by preexisting spectroscopic surveys (e.g., SDSS). So a complete spectroscopic sample (as used in this work) in the GAMA sky area includes those observed by both the GAMA team and other preexisting surveys (Driver et al. 2011).

To measure the size of CSSs that are usually marginally resolved in ground-based images, we turn to the Hyper Suprime-Cam Subaru Strategic Program (HSC-SSP; Aihara et al. 2018) wide-layer imaging survey, which surpasses previous surveys in its combination of sky coverage and imaging quality (e.g., i-band seeing $\sim 0\farcs6$; $r_{\rm limit} \simeq 26$ mag). The GAMA fields G09, G12, G15, and part of G02 fall within the sky coverage of the latest data release of HSC-SSP (DR3; Aihara et al. 2022), with an overlapping area of ~ 200 deg^2 in total. Our CSS sample is selected from this overlapping sky area of GAMA and HSC-SSP (hereafter GAMA-HSC).

The selection procedure starts from all GAMA-HSC objects with heliocentric velocities > 500 km s^{-1} and redshift < 0.1[7]. Then, we measure the effective radii R_e of these objects with GALFIT (Peng et al. 2010) by adopting single Sérsic models. The median of the R_e measured in all available bands is used in our analysis. Our experiments suggest that reliable R_e can be measured with GALFIT down to $1/3 \times$ the FWHM of the point spread function (PSF) within 20% uncertainties (see Appendix appendix for more details). For the unresolved objects (i.e., $R_e < 1/3 \times$ the FWHM of the PSF), we conservatively adopt half the FWHM of the PSF as the upper limit of R_e. We select objects with $R_e < 600$ pc following previous searches of CSSs (e.g., Norris et al. 2014; Chilingarian & Zolotukhin 2015; Kim et al. 2020; Rey et al. 2021). Next, we exclude objects that fall above the lower boundary of the 95% range of the size–magnitude distribution of ordinary dwarf galaxies, as illustrated by the green shaded region in Figure 1. Lastly, we carry out a visual inspection of images of the above-selected CSS candidates to exclude H II regions that are part of other galaxies.
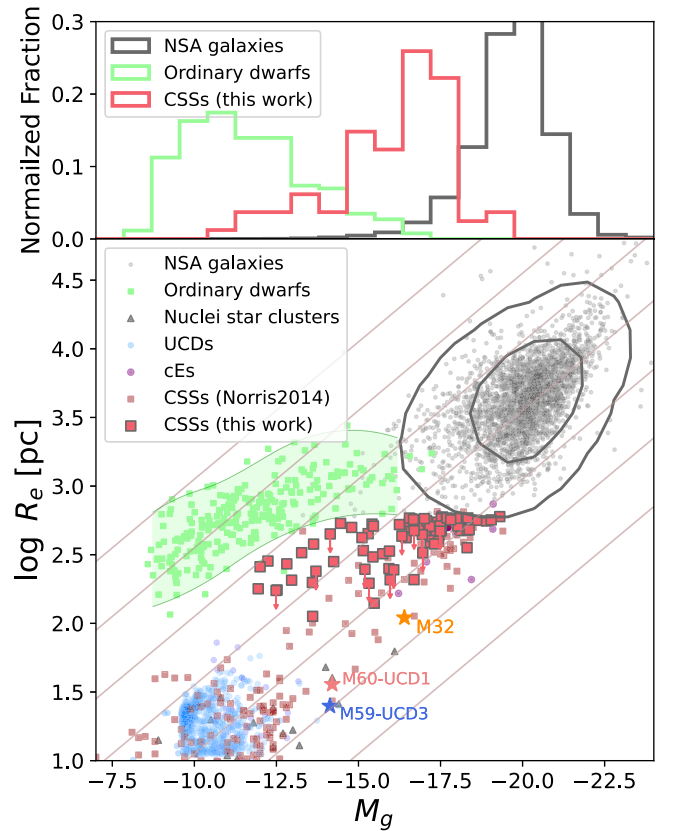

Figure 1. Upper panel: g-band absolute magnitude distributions for galaxies from the NASA Sloan Atlas catalog (NSA; Blanton et al. 2011) within the same redshift range as our sample for ordinary dwarf galaxies from Eigenthaler et al. (2018), and for CSSs in this work, are plotted as gray, green, and red histograms, respectively. Lower panel: R_e–M_g distribution. Red squares represent our CSSs and symbols with arrows attached indicate unresolved CSSs. The black contours enclose the central 68% and 95% of NSA galaxies. Only 3000 randomly chosen galaxies in the NSA catalog are plotted (gray dots). The green shaded region encloses 95% of ordinary dwarf galaxies. Nuclear star clusters (Brodie et al. 2011; Misgeld & Hilker 2011) are plotted as filled triangles. UCDs (Zhang et al. 2015; Liu et al. 2020; Saifollahi et al. 2021) and cEs (Huxor et al. 2013; Paudel et al. 2014; Guérou et al. 2015) are plotted as blue and purple dots, respectively. CSSs from Norris et al. (2014) are plotted as small brown squares. M32, M60-UCD1 (Strader et al. 2013), and M59-UCD3 (Liu et al. 2015b) are plotted as filled stars. The diagonal lines represent constant g-band surface brightness.

The above selection procedure results in a sample of 395 CSSs candidates. By using a demarcation at log sSFR $= -11$, where sSFR $\equiv$ SFR$/M_\star$ (see Section 3.2), we divide the sample into 313 star-forming and 82 quiescent CSSs, 12 of which are unresolved. None of our CSSs exhibits broad emission lines that would be a signature of Type 1 active galactic nuclei (AGNs). The smallest heliocentric velocity of this sample turns out to be 887 km s^{-1}. We will focus on the 82 quiescent CSSs (hereafter CSSs for brevity) in the rest of the paper. Figure 1 shows the size–magnitude distribution of our CSSs (red data points).

It is worth noting that any large-scale spectroscopic galaxy surveys inevitably miss some of the most compact galaxies (with respect to spatial resolution) in order to maintain reasonable survey efficiency. Nevertheless, GAMA makes an effort to significantly alleviate this potential issue by relaxing the star–galaxy separation criteria for the input catalog of photometric candidates. According to Baldry et al. (2010), GAMA is nearly complete at $\Delta_{\rm sg} > 0.05$ mag, where $\Delta_{\rm sg}$ is the

---

[7] Only objects with redshift quality flag $nQ \geqslant 3$ are considered for our analysis, following Liske et al. (2015).

PSF minus model magnitude difference. For comparison, the completeness limit of the SDSS main survey is $\Delta_{\rm sg} > 0.24$ mag. It is not straightforward to estimate the fraction of potentially missed CSSs due to the $\Delta_{\rm sg}$ limit imposed by GAMA. However, we point out that our conclusion in this paper would not change if the $\Delta_{\rm sg}$ limit is raised, for instance, to $\Delta_{\rm sg} > 0.24$ (including 63, or 77%, of our CSSs).

2.2. Control Sample of Ordinary Galaxies

We also select a control sample of ordinary quiescent galaxies from the same sky fields of GAMA. For each CSS in our sample, we randomly select an ordinary galaxy that has log SFR and $\log M_\star$ that are each within ± 0.3 dex of the CSS. Here the "ordinary" galaxies are defined to be above the upper boundary of our CSS sample on the $R_{\rm e}$–M_g plane. We have repeated the random sampling of ordinary galaxies for several tens of times and found that the relevant conclusion for the control sample in this work does not vary. So, the following analysis will be based on one of these randomly selected control sample.

3. Analysis

3.1. Quantifying the Local Environment

To quantify the local environment, we derive $\log D/R_{\rm vir}$ for both the CSS and control samples, where D is the projected distance to the nearest luminous neighboring galaxy that is at least 2.0 mag more luminous and has a radial velocity within $\pm 500\,{\rm km\,s^{-1}}$ of the galaxy in question, and $R_{\rm vir}$ is the virial radius of the selected luminous neighbor, approximated to be 67 times its effective radius (Kravtsov 2013). We note that $\log D/R_{\rm vir}$ was derived by requiring the nearest luminous neighbor to have $M_r < -21$ mag in Kim et al. (2020). We also calculate $\log D/R_{\rm vir}$ for our samples in the same way as Kim et al. (2020) in order to check the influence of different definitions on our results. As will become clear in Section 4.1, the sample can be divided into field and satellite subsamples, with a demarcation at $D/R_{\rm vir} \simeq 0.4$.

We also derive the projected galaxy number density parameter: $\eta_k = \log(\frac{3(k-1)}{4\pi d_k^3})$ (Argudo-Fernández et al. 2015), where d_k is the projected distance to the fifth (i.e., $k = 5$) nearest galaxy in Mpc. Only neighbors with $M_r < -18.6$ are considered in the η_k calculation, corresponding to the GAMA completeness limit (i.e., $r = 19.72$ mag) at the distance of the most distant CSS in our sample.

Lastly, we mention that 22 of the 82 CSSs belong to groups with at least 10 member galaxies according to the GAMA galaxy group catalog (G3C; Robotham et al. 2011).

3.2. Stellar Population Modeling

Stellar masses of our CSSs are estimated by fitting broadband spectral energy distribution with the Code Investigating GALaxies Emission (CIGALE; Boquien et al. 2019), using the optical photometry from SDSS and HSC-SSP and near-infrared photometry from the Wide-field Infrared Survey Explorer (WISE; Wright et al. 2010). Star formation rates (SFRs) are estimated from Hα luminosities offered by GAMA DR4 by adopting the formula $\log {\rm SFR}[M_\odot\,{\rm yr}^{-1}] = \log L({\rm H}\alpha)[{\rm erg\ s}^{-1}] - 41.27$ (Kennicutt & Evans 2012), where Hα is corrected for internal dust extinction from the Balmer decrement by assuming an intrinsic flux ratio of $({\rm H}\alpha/{\rm H}\beta) = 2.86$.

Luminosity-weighted stellar ages and metallicities [Z/H] are estimated by performing a joint fitting of the (Gaussian) emission lines (if any) and spectral continuum (3540 Å–5700 Å) of the spectra with the Penalized PiXel-Fitting (pPXF; Cappellari 2017) package by using the MILES stellar library and nonparametric star formation histories. The individual spectrum was corrected for the Galactic extinction (Schlegel et al. 1998) and shifted to the rest frame before the fitting.

4. Results

4.1. Environmental Distribution

The distribution of the environmental parameters of our CSSs and the control sample (Section 3.1) are shown in Figure 2. The CSSs appear to follow a bimodal $\log D/R_{\rm vir}$ distribution, with one group of CSSs peaking around $\log D/R_{\rm vir} \sim -1$ and the other group peaking around $\log D/R_{\rm vir} \sim 1$. In contrast to the CSSs, the control sample appears to follow a unimodal distribution, which peaks at $\log D/R_{\rm vir}$ in between the two groups of CSSs. The projected number density η_k distribution appears to be unimodal for both samples. To verify this visual impression, we turn to the Python implementation of Gaussian Mixture Models (GMM) and use the Bayesian information criterion (BIC) to select the minimum number $N_{\rm comp}$ of Gaussian components that can adequately describe the observed distributions.

The GMM fitting results are illustrated in Figure 2. For CSSs, the BIC reaches minimum at $N_{\rm comp} = 2$. With Δ(BIC) $\simeq -40$ (for our default luminous neighbor selection method; left panel) or -30 (for the Kim et al. 2020 method; middle panel), the two-component models are strongly favored against one-component models. The two best-fit Gaussian subcomponents of the CSSs intersect at $\log D/R_{\rm vir} \sim -0.4$. For the control sample, the BIC reaches minimum at $N_{\rm comp} = 1$, verifying their unimodal distribution. The GMM fitting also verifies the visual impression of unimodal η_k distributions for both samples.

4.2. Structural Properties of CSSs and Their Hosts

Given the above results, we split our CSSs into field and satellite subsamples by using $\log D/R_{\rm vir} = -0.4$.

The stellar size–mass distributions of the subsamples are exhibited in Figure 3. Number density contours that enclose 68% of the CSSs in each subsample are overplotted to guide the comparison between the subsamples. As indicated by the parallel lines of equal surface mass densities, the satellite CSSs cover a surface mass density range of $2 \lesssim \log \Sigma_{\rm e}[M_\odot/{\rm pc}^2] \lesssim 4$ on the size–mass plane. The distribution of the field subsample is clustered at a similar surface mass density range, albeit with a tail extending to lower mass densities.

To probe the morphologies of the nearest luminous neighboring galaxies of the satellite CSSs, we use the Sérsic indices (n) provided by the NSA catalog to classify the neighbors into early-type galaxies (ETGs; $n > 2.5$) and late-type galaxies (LTGs; $n < 2.5$). Not all of the neighboring galaxies have n measurements. For those with n measurements, 83% (20) of the satellite CSSs have ETG neighbors. This finding is in line with the well-known "galactic conformity" phenomenon (Weinmann et al. 2006).
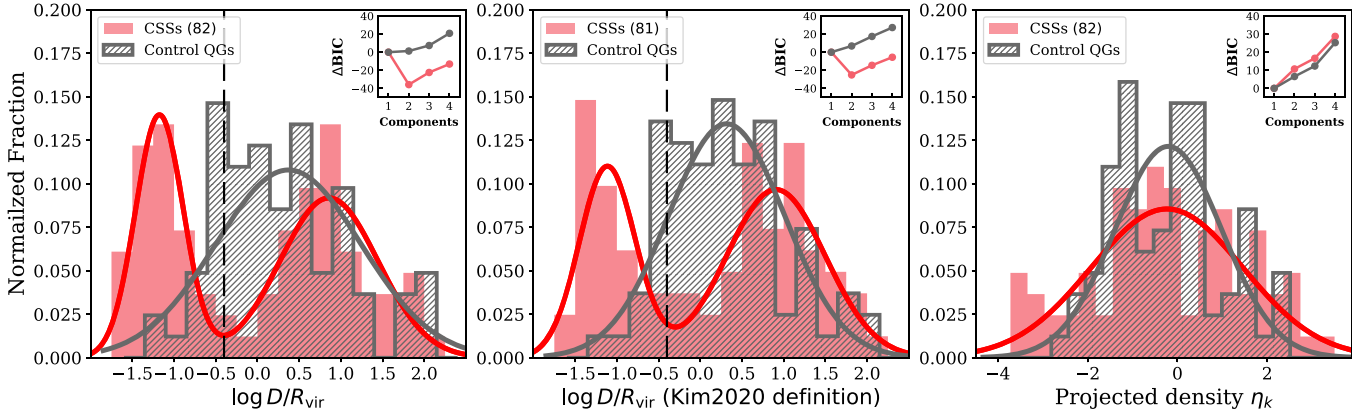
Figure 2. Normalized distribution of the environmental parameters of CSSs (red filled histogram) and control sample (gray hatched histogram). The left panel is for the projected distances to the nearest luminous neighboring galaxy selected with the default method described in the text, and the middle panel is for the projected distances to the nearest luminous neighboring galaxy selected with the method in Kim et al. (2020). The projected distances have been normalized by the virial radii of the selected nearest neighbors. The right panel shows the distributions of the projected number density of nearby galaxies. The best-fit Gaussian curves from the GMM fit to each sample are overplotted on the histograms. The inset figure in each panel shows the $\Delta \mathrm{BIC} \equiv \mathrm{BIC}(\mathrm{Component} = n) - \mathrm{BIC}(\mathrm{Component} = 1)$ for a GMM fit with a different number n of components. See Section 3.1 for details of the environmental parameters plotted here.
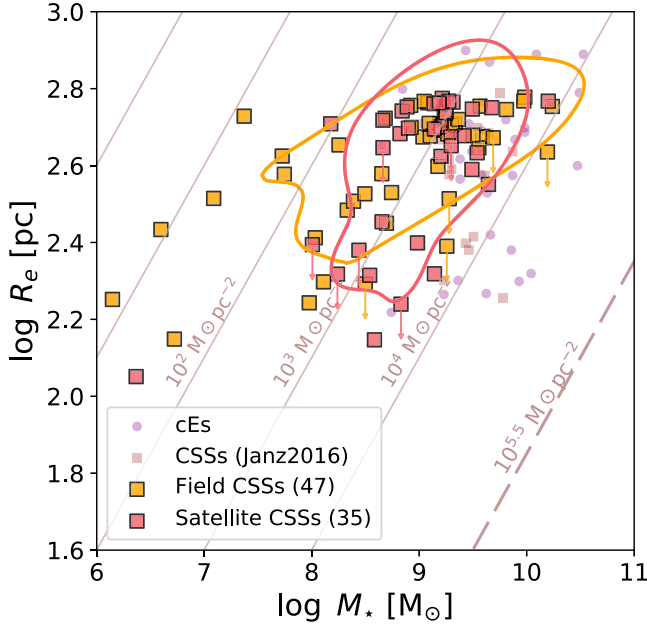
Figure 3. Size–mass distribution of our CSSs. Iso-number density contours that enclose 68% of the field and satellite CSSs are overplotted with the same color scheme as the data points. The arrows indicate unresolved CSSs. Literature cEs (Guérou et al. 2015; Ferré-Mateu et al. 2018) and CSSs (Janz et al. 2016) are plotted as purple dots and brown squares, respectively. Lines of iso-$\Sigma_e \equiv M_\star / (2\pi R_e^2)$ are indicated by brown slanted lines. The brown dashed line represents the maximum effective stellar mass density ($\Sigma_{\max} \simeq 10^{5.5} M_\odot \, \mathrm{pc}^{-2}$) expected for CSSs in the local universe (Hopkins et al. 2010).

Figure 4. Age$-[Z/H]$ diagram. The median values of the field and satellite subsamples of our CSSs are shown as big filled squares. The contour curves enclose 68% of the CSSs in each of our subsamples. Literature CSSs (Janz et al. 2016) or cEs (Chilingarian & Zolotukhin 2015; Guérou et al. 2015; Ferré-Mateu et al. 2018; Kim et al. 2020) are plotted with symbols indicated in the legend. The error bars of the median values of our CSSs are determined by random resampling of the original subsamples with replacement for 1000 times.

4.3. Stellar Populations of CSSs

Luminosity-weighted stellar ages and metallicities of the field and satellite subsamples of CSSs are shown separately in Figure 4. Contours that enclose 68% of the CSSs in each subsample, and the median values are indicated in Figure 4. Literature samples of cEs are also plotted for comparison purposes. Our CSSs cover nearly the same ranges of age and metallicities as the literature cEs. The satellite CSSs have significantly older median ages and higher median metallicities than the field CSSs. Systematically higher metallicities for satellite cEs were also reported by Kim et al. (2020).
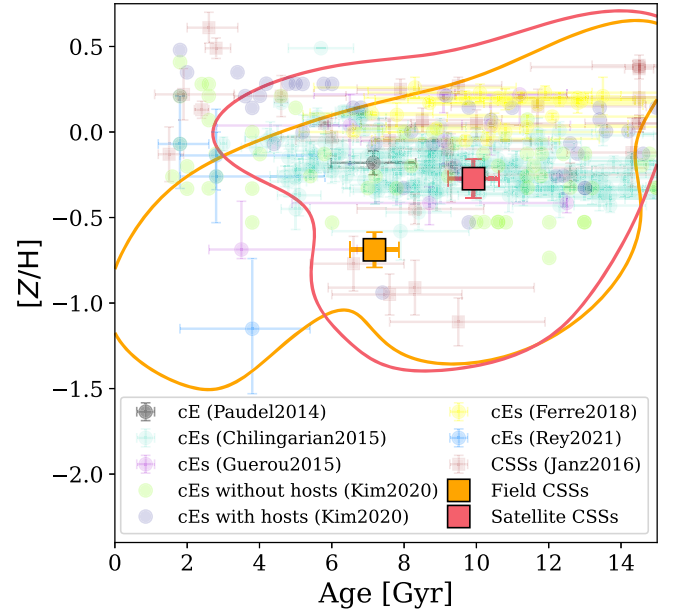
5. Summary and Discussion

We have taken a complete (in a flux-limited sense) census of quiescent CSSs over a total sky area of $\sim 200 \deg^2$ at $z < 0.1$. The sky area was observed by the spectroscopic survey of GAMA and the wide-field imaging survey of HSC-SSP. GAMA largely overcomes the fiber-collision problem that has plagued the census of galaxies at small scales for most existing large-area spectroscopic surveys and thus provides a unique opportunity to explore the environmental dependence of the formation of CSSs in an unbiased way. We selected 82 quiescent CSSs and studied their small-scale environmental distribution, structural properties, and stellar populations.

We quantify the local environment by using the normalized projected distance (D/R_{vir}) to the nearest luminous neighboring galaxy and find that these CSSs have a bimodal distribution, with one peak near $\sim 0.1 \times R_{vir}$ and the other peak near $\sim 10 \times R_{vir}$. Such bimodal distribution is not seen in ordinary quiescent galaxies.

We divide the CSSs into field and satellite subsamples based on their bimodal D/R_{vir} distribution and find that the field and satellite CSSs follow similar mass–size distributions. Based on full-spectrum stellar population fitting, we find that the satellite CSSs are older and more metal-rich than field CSSs on average. A majority (83%) of satellite CSSs have early-type hosts.

The majority (85%; Figure 3) of our CSSs fall within the stellar mass range of cEs (10^8–10^{10} $M_\odot$). A closely relevant study by Kim et al. (2020) found an environmental dependence on the metallicity distribution of cEs, i.e., satellite cEs (especially those inhabiting rich groups), tend to have higher metallicities than field cEs of comparable masses, while field cEs largely follow the mass–metallicity relation of massive ordinary ETGs. A natural explanation for the different metallicity distributions is that, first, satellite cEs have experienced tidal stripping that significantly reduced the mass but barely affected the metallicities, and second, field cEs may be born to be the low-mass extension of more massive ellipticals. Our finding of the bimodal D/R_{vir} distribution of quiescent CSSs reinforces the existence of two distinct formation channels of cEs (e.g., Huxor et al. 2011; Janz et al. 2016; Ferré-Mateu et al. 2018).

The fact that a bimodal distribution instead of a skewed unimodal distribution is observed for the CSSs may be understood from two plausible perspectives. First, in the tidal stripping framework, substantial tidal stripping happens only when satellites travel sufficiently close to the massive host (e.g., Pfeffer & Baumgardt 2013; Mayes et al. 2021). Second, in the hierarchical structure formation framework, CSSs inhabit higher-density subhalos than do the ordinary satellites and thus have a higher degree of central concentration toward massive halos (e.g., Diemand et al. 2005).

Appendix A
Test of the Effective Radius Measurements

We use mock galaxies to evaluate the limitation of HSC-SSP images for measuring the R_e of nearby CSSs. The test results are shown in Figure 5. Specifically, we use the best-fit double-Sérsic parameters of the compact elliptical NGC 5846cE (Chilingarian & Bergond 2010) and a series of single-Sérsic profiles with different Sérsic indices to create PSF-convolved mock galaxy images for the test. The mock galaxies have intrinsic $R_e = 240$ pc and V-band absolute magnitude of -17.07 mag. Each of the mock galaxies is put at a range of redshifts and randomly placed at blank sky regions of the HSC-SSP images. We use GALFIT to fit these mock galaxies with either single (filled symbols in Figure 5) or double (open symbols) Sérsic components and compare the output R_e to the input in Figure 5. Given this test, a single-Sérsic GALFIT fitting can recover R_e to within 20% at a limit of $R_e > 1/3$ PSF FWHM, below which the galaxies are regarded to be unresolved.
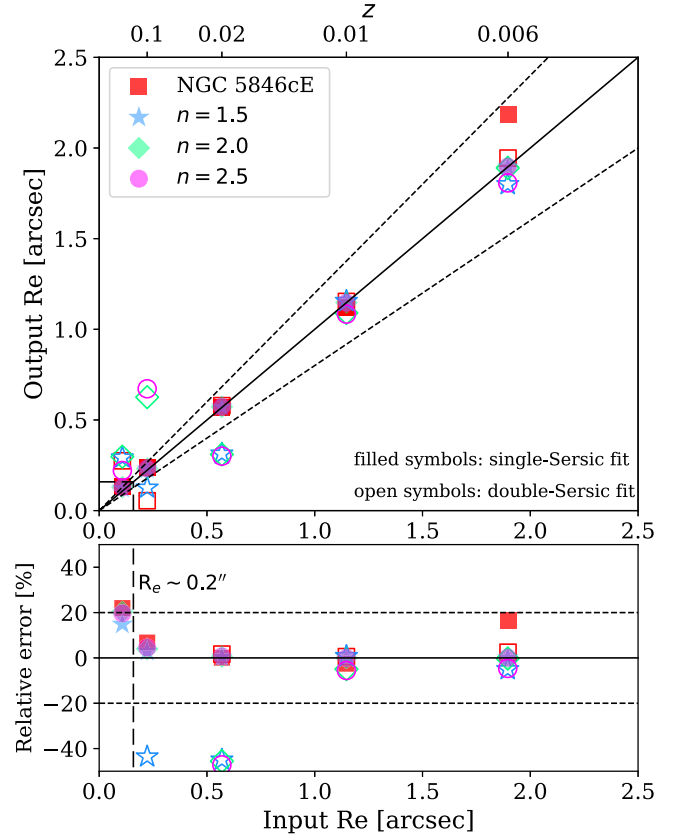

Figure 5. Comparison of the input and best-fit R_e (by GALFIT) of mock galaxies. The squares correspond to mock galaxies with the same structural parameters with the cE NGC 5846cE, and the other symbols correspond to single-Sérsic mock galaxies with different Sérsic indices n. The same mock galaxies are put at a series of redshift, i.e., 0.1, 0.05, 0.02, 0.01, and 0.006. The filled (open) symbols correspond to GALFIT fitting with single (double) Sérsic functions. The vertical dashed lines indicate the R_e measurement limit adopted in our work, which is about $1/3 \times$ PSF FWHM. Note that a Gaussian distribution has $R_e \simeq 1/2 \times$ FWHM.

ORCID iDs

Guangwen Chen https://orcid.org/0000-0002-4742-8800
Hong-Xin Zhang https://orcid.org/0000-0003-1632-2541
Xu Kong https://orcid.org/0000-0002-7660-2273
Zesen Lin https://orcid.org/0000-0001-8078-3428
Zhixiong Liang https://orcid.org/0000-0002-2384-3436
Zuyi Chen https://orcid.org/0000-0002-2178-5471
Yimeng Tang https://orcid.org/0000-0003-2876-577X
Xinkai Chen https://orcid.org/0000-0002-5016-6901

References

Aihara, H., AlSayyad, Y., Ando, M., et al. 2022, PASJ, 74, 247
Aihara, H., Arimoto, N., Armstrong, R., et al. 2018, PASJ, 70, S4
Argudo-Fernández, M., Verley, S., Bergond, G., et al. 2015, A&A, 578, A110
Baldry, I. K., Robotham, A. S. G., Hill, D. T., et al. 2010, MNRAS, 404, 86
Blanton, M. R., Kazin, E., Muna, D., Weaver, B. A., & Price-Whelan, A. 2011, AJ, 142, 31
Boquien, M., Burgarella, D., Roehlly, Y., et al. 2019, A&A, 622, A103
Brodie, J. P., Romanowsky, A. J., Strader, J., & Forbes, D. A. 2011, AJ, 142, 199
Cappellari, M. 2017, MNRAS, 466, 798
Chilingarian, I., Cayatte, V., Revaz, Y., et al. 2009, Sci, 326, 1379
Chilingarian, I., & Zolotukhin, I. 2015, Sci, 348, 418
Chilingarian, I. V., & Bergond, G. 2010, MNRAS, 405, L11
Diemand, J., Madau, P., & Moore, B. 2005, MNRAS, 364, 367
Drinkwater, M. J., Jones, J. B., Gregg, M. D., & Phillipps, S. 2000, PASA, 17, 227
Driver, S. P., Bellstedt, S., Robotham, A. S. G., et al. 2022, MNRAS, 513, 439
Driver, S. P., Hill, D. T., Kelvin, L. S., et al. 2011, MNRAS, 413, 971
Du, M., Debattista, V. P., Ho, L. C., et al. 2019, ApJ, 875, 58
Eigenthaler, P., Puzia, T. H., Taylor, M. A., et al. 2018, ApJ, 855, 142
Fellhauer, M., & Kroupa, P. 2002, MNRAS, 330, 642
Ferré-Mateu, A., Forbes, D. A., Romanowsky, A. J., Janz, J., & Dixon, C. 2018, MNRAS, 473, 1819

Guérou, A., Emsellem, E., McDermid, R. M., et al. 2015, ApJ, 804, 70
Hilker, M., Infante, L., & Richtler, T. 1999, A&AS, 138, 55
Hopkins, P. F., Murray, N., Quataert, E., & Thompson, T. A. 2010, MNRAS, 401, L19
Huxor, A. P., Phillipps, S., & Price, J. 2013, MNRAS, 430, 1956
Huxor, A. P., Phillipps, S., Price, J., & Harniman, R. 2011, MNRAS, 414, 3557
Janz, J., Norris, M. A., Forbes, D. A., et al. 2016, MNRAS, 456, 617
Kennicutt, R. C., & Evans, N. J. 2012, ARA&A, 50, 531
Kim, S., Jeong, H., Rey, S.-C., et al. 2020, ApJ, 903, 65
Kravtsov, A. V. 2013, ApJL, 764, L31
Liske, J., Baldry, I. K., Driver, S. P., et al. 2015, MNRAS, 452, 2087
Liu, C., Côté, P., Peng, E. W., et al. 2020, ApJS, 250, 17
Liu, C., Peng, E. W., Côté, P., et al. 2015a, ApJ, 812, 34
Liu, C., Peng, E. W., Toloba, E., et al. 2015b, ApJL, 812, L2
Mayes, R. J., Drinkwater, M. J., Pfeffer, J., et al. 2021, MNRAS, 501, 1852
Mieske, S., Hilker, M., & Misgeld, I. 2012, A&A, 537, A3
Misgeld, I., & Hilker, M. 2011, MNRAS, 414, 3699
Norris, M. A., Kannappan, S. J., Forbes, D. A., et al. 2014, MNRAS, 443, 1151
Paudel, S., Lisker, T., Hansson, K. S. A., & Huxor, A. P. 2014, MNRAS, 443, 446
Pechetti, R., Seth, A., Kamann, S., et al. 2022, ApJ, 924, 48
Peng, C. Y., Ho, L. C., Impey, C. D., & Rix, H.-W. 2010, AJ, 139, 2097
Pfeffer, J., & Baumgardt, H. 2013, MNRAS, 433, 1997
Price, J., Phillipps, S., Huxor, A., et al. 2009, MNRAS, 397, 1816
Rey, S.-C., Oh, K., & Kim, S. 2021, ApJL, 917, L9
Robotham, A. S. G., Norberg, P., Driver, S. P., et al. 2011, MNRAS, 416, 2640
Saifollahi, T., Janz, J., Peletier, R. F., et al. 2021, MNRAS, 504, 3580
Schlegel, D. J., Finkbeiner, D. P., & Davis, M. 1998, ApJ, 500, 525
Seth, A. C., van den Bosch, R., Mieske, S., et al. 2014, Natur, 513, 398
Strader, J., Seth, A. C., Forbes, D. A., et al. 2013, ApJL, 775, L6
Weinmann, S. M., van den Bosch, F. C., Yang, X., & Mo, H. J. 2006, MNRAS, 366, 2
Wright, E. L., Eisenhardt, P. R. M., Mainzer, A. K., et al. 2010, AJ, 140, 1868
York, D. G., Adelman, J., Anderson, J. E. J., et al. 2000, AJ, 120, 1579
Zhang, H.-X., Peng, E. W., Côté, P., et al. 2015, ApJ, 802, 30
Zhang, H.-X., Puzia, T. H., Peng, E. W., et al. 2018, ApJ, 858, 37